Adaptive Displacement Calibration Strategies for Field Structural Health Monitoring Based on Doppler Radars

Davi V. Q. Rodrigues, *Student Member, IEEE*, Delong Zuo, Ziyan Tang, Jing Wang, *Student Member, IEEE*, Changzhan Gu, *Senior Member, IEEE*, and Changzhi Li, *Senior Member, IEEE*

***Abstract*— This article presents two displacement calibration algorithms for Doppler radar demodulated data, which contribute to accurate monitoring of small vibrations even when the conventional arctangent demodulated displacement exhibits abrupt jumps. The field structural health monitoring of a traffic signal support structure was carried out by a 5.8-GHz Doppler radar to verify the effectiveness of each algorithm. The radar sensor captures and downconverts the microwave signal, which is phase modulated by the mast arm motion after being reflected on the ground. When conventional nonlinear phase demodulation is employed to retrieve the mast arm displacement from the Doppler radar baseband responses, sudden jumps are encountered in the displacement measurement. Two novel algorithms, referred to as the adaptive low-pass filtering algorithm (ALFA) and the adaptive joint signal processing algorithm (AJSPA), respectively, are suggested to eliminate jumps in phase-demodulated Doppler radar data. These strategies are compared in terms of accuracy and computational cost. The simulated and experimental results are provided to validate the proposed techniques. The presented methods can have wide applications in radar-based vibration monitoring.**

***Index Terms*— Displacement measurement, Doppler radar, nonlinear phase demodulation, remote sensing, structural health monitoring (SHM).**

I. Introduction

STRUCTURAL health monitoring (SHM) is the process of continuously observing the integrity of structures, such as bridges, high-rise buildings, and dams, in order to extend their useful life, reduce maintenance costs, and improve public safety [1]. Cracks, corrosion, and loss of connections may change the natural frequency and mode shapes of civil infrastructures, provoking its abnormal operation. Traffic signal support structures are in a strong need for SHM to enable timely maintenance in order to avoid catastrophic failures such as abrupt fracture. Indeed, bearing the self-weight of a horizontal arm and the dynamic loads from wind excitation, the junction of a traffic signal support structure has been observed to be susceptible to fatigue damage [2].

As the aging of worldwide critical infrastructures raises concerns, advances in SHM technologies have been pursued over the past few decades. Conventional SHM can be accomplished in several ways. Accelerometers, which are relatively cost-effective and can be readily instrumented, have been frequently used for vibration measurements [3]. Nevertheless, the twice integration of acceleration data contributes to errors added to the displacement measurement. Eddy-current proximity sensors, laser sensors, and vision-based sensors are three representatives of noncontact solutions for SHM. However, these sensors have practical limitations. Eddy-current displacement sensors and laser displacement sensors are both sensitive to the measurement range and the surface condition of the objects [4]–[6]. Vision-based sensors demand large computational resources for image recognition and have dependence on lighting conditions [7]–[9].

Researchers have applied Doppler radar systems for animal and human noncontact vital sign detection, monitoring of sleep apnea, and accurate tumor tracking in lung cancer radiotherapy [10]–[14]. Doppler radar sensors are attractive for their robustness against weather condition and ambient light, longer monitoring range, and noncontact operation. Benefiting from the ability to provide accurate low-frequency displacement measurement, short-range microwave Doppler radars have emerged as a potential solution for monitoring the health of civil infrastructures, such as historical buildings and bridges [15]–[20]. In addition, the potential cost of Doppler radar sensors after CMOS integration and mass production could be much lower than the costs associated with cameras and laser vibrometers. Radar sensors may be solely employed or combined employed in wireless smart sensor networks to detect structural deflections [21]–[23]. Furthermore, with the growing interest in sustainable energy, an increment in the number and size of wind turbines brings the necessity of SHM for them, and noncontact radar technologies can provide complementary alternative to the existing solutions.

Manuscript received November 22, 2019; revised February 8, 2020; accepted March 8, 2020. Date of publication March 27, 2020; date of current version September 15, 2020. This work was supported by the National Science Foundation (NSF) under Grant ECCS-1808613 and Grant CNS-1718483. The Associate Editor coordinating the review process was Huang-Chen Lee. *(Corresponding author: Davi V. Q. Rodrigues.)*

Davi V. Q. Rodrigues, Jing Wang, and Changzhi Li are with the Department of Electrical and Computer Engineering, Texas Tech University, Lubbock, TX 79409 USA (e-mail: davi.rodrigues@ttu.edu; anna.wang@ttu.edu; changzhi.li@ttu.edu).

Delong Zuo is with the Department of Civil, Environmental and Construction Engineering, Texas Tech University, Lubbock, TX 79409 USA (e-mail: delong.zuo@ttu.edu).

Ziyan Tang is with the Department of Mechanical Engineering, University of Michigan, Ann Arbor, MI 48109 USA (e-mail: tomtang@umich.edu).

Changzhan Gu is with the Department of Electronic Engineering, Artificial Intelligence Institute, Shanghai Jiao Tong University, Shanghai 200240, China (e-mail: changzhan@sjtu.edu.cn).

Color versions of one or more of the figures in this article are available online at http://ieeexplore.ieee.org.

Digital Object Identifier 10.1109/TIM.2020.2982233

Early detection of the rupture of the blade tips or of damages in the yaw-bearing system may prevent serious disasters, especially in earthquake-sensitive areas. Short-range Doppler radar signatures of industrial wind turbines have been analyzed and verified, introducing a new form of SHM for those infrastructures using portable Doppler radar systems [24]–[26].

To tackle potential barriers for practical implementations and obtain robust performance, signal processing methods, such as adaptive dc calibration, have been proposed [27]–[29]. It should be mentioned that the dc offset calibration methods play an important role in data demodulation for SHM based on quadrature architecture Doppler radars. The accuracy of the radar displacement measurement relies on the successful application of the dc offset calibration algorithm. In addition, data-processing costs must be considered when developing embedded software for SHM sensors with limited power and computational capabilities [28].

This article addresses another challenge for SHM based on Doppler radars. It was noted that sudden jumps are introduced in the demodulated displacement measurement when a 5.8-GHz Doppler radar was employed to monitor the mast arm motion of a traffic signal support structure. To overcome this challenge, this article proposes an adaptive low-pass filtering algorithm (ALFA) and an adaptive joint signal processing algorithm (AJSPA). Both algorithms are presented and evaluated, and their automated realizations are revealed. In addition to the accuracy, computational efficiency for each approach is discussed. The procedures described in this article are an extension of the published results in [30], which presented the major cause of sudden jumps when extracting oscillatory displacement from the phase history of the Doppler radar data and introduced the joint signal processing algorithm (JSPA). However, the manual adjustment of the JSPA's parameters impedes its practical application. To overcome the abovementioned challenge, this article proposes an adaptive approach to improve the previous JSPA and presents another method based on adaptive low-pass filtering. To the best of our knowledge, the issue of the sudden jumps in Doppler phase-demodulated data has never been addressed, which highlights the main contribution of this article.

The remainder of this article is organized as follows. Section II elaborates the theoretical formulation of Doppler radar on field SHM applications. Section III addresses the problem of interest and shows the drawback of the conventional demodulation algorithm for field SHM. Furthermore, it details the displacement measurement calibration methods and presents the simulation results that validate the theoretical framework. Then, the field experimental setup and the obtained measurement results are described in Section IV. A comparative study between the two algorithms is provided in Section V. The conclusions of this article are drawn in Section VI.

II. Theory

The 5.8-GHz Doppler radar is housed in a waterproof enclosure and attached to the bottom side of the traffic signal's mast arm with its two antennas pointing downward. The block diagram for the field SHM based on Doppler radar is shown in Fig. 1. A continuous-wave signal $T(t)$ is transmitted toward the ground, where it is phase-modulated due to the mast arm motion. Then, the radio frequency (RF) reflected signal $R(t)$ is amplified and converted into baseband $I(t)$ and $Q(t)$ signals using a quadrature mixer, after being captured by the receiver. An accelerometer provides the ground truth.

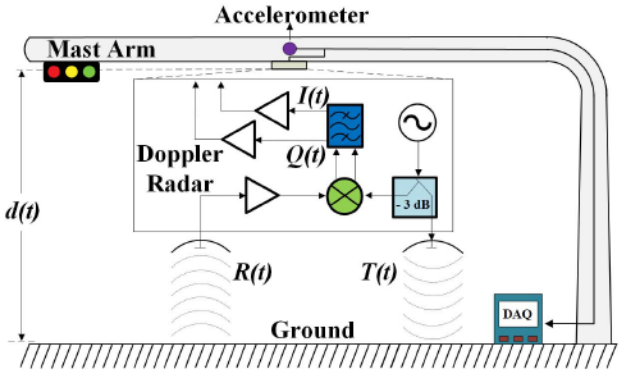

Fig. 1. Block diagram for field SHM based on Doppler radar.

A. Theory of Doppler Radar for SHM

The transmitted signal has the usual form of

$$T(t) = \cos(\omega t + \varphi(t)) \tag{1}$$

where $\omega = 2\pi f$ represents the angular frequency of the RF carrier.

The mast arm is located at a nominal distance of d_0 above the ground with a displacement $x(t)$, which can be approximated as a sinusoid with time-varying amplitude m and angular dominant frequency ω_0. Therefore, $x(t)$ can be expressed as

$$x(t) = m\sin(\omega_0 t). \tag{2}$$

The total distance traveled by the RF continuous-wave signal between the transmitting and receiving antennas is $2d(t)$, where $d(t) = d_0 + x(t)$. The transmitted signal is reflected by the ground. After the round-trip travel of the transmitted signal, the amplitude-normalized received signal $R(t)$ can be written as

$$R(t) \approx \cos\left(\omega t - \frac{4\pi d_0}{\lambda} - \frac{4\pi x(t)}{\lambda} + \varphi\left(t - \frac{2d(t)}{c}\right)\right) \tag{3}$$

where c denotes the speed of light and $\lambda = c/f$ is the free-space wavelength. Quadrature baseband outputs $I(t)$ and $Q(t)$ are extracted by downconverting $R(t)$ using the same transmitted signal as a reference and may be analyzed by a spectral analysis as follows [31]:

$$\begin{aligned} I(t) &= \cos\left(\frac{4\pi x(t)}{\lambda} + \frac{4\pi d_0}{\lambda} + \Delta\theta(t)\right) + \mathrm{DC}_I \\ &= \sum_{p=-\infty}^{\infty} J_p\left(\frac{4\pi m}{\lambda}\right)\cos\left(p\omega_0 t + \Delta\phi(t)\right) + \mathrm{DC}_I \end{aligned} \tag{4}$$

$$\begin{aligned} Q(t) &= \sin\left(\frac{4\pi x(t)}{\lambda} + \frac{4\pi d_0}{\lambda} + \Delta\theta(t)\right) + \mathrm{DC}_Q \\ &= \sum_{p=-\infty}^{\infty} J_p\left(\frac{4\pi m}{\lambda}\right)\sin\left(p\omega_0 t + \Delta\phi(t)\right) + \mathrm{DC}_Q \end{aligned} \tag{5}$$

where J_p is the pth order Bessel function of the first kind, $\Delta\theta(t)$ is the total residual phase noise, and $\Delta\phi(t) = 4\pi d_0/$

$\lambda + \Delta\theta(t)$. It can be seen from (4) and (5) that the periodic baseband signals are represented not only by a single tone but also by a sum of infinite sinusoidal components at harmonic frequencies of the displacement fundamental frequency ω_0. Moreover, the Bessel coefficients of each harmonic component are a function of the instantaneous motion amplitude. It can even vanish under certain values of m.

A dc offset removal algorithm must condition the I/Q baseband signal responses for phase demodulation. DC_I and DC_Q, which are caused by circuit imperfections and the reflection from stationary clutters, must be eliminated. Moreover, the I and Q amplitudes must be normalized, and the location of the I/Q trajectory may be adjusted, using the measured data to find its centroid. Then, the displacement measurement is acquired after the arctangent demodulation, which recovers the angular information and calculates the phase shift for each of the two adjacent points. Phase unwrapping is necessary to correct the phase discontinuity when the signal trajectory crosses the boundary between two adjacent quadrants of the I/Q constellation graph [32].

III. Adaptive Low-pass Filtering Algorithm and Adaptive Joint Signal Processing Algorithm

Phase distortion can significantly affect the accuracy of Doppler radar displacement measurements. As a matter of fact, for the SHM of a traffic signal structure, the long distance between the mast arm and the ground surface and the open environment lead to strong clutter noises coupled into the Doppler radar system. Furthermore, the instantaneous magnitude of the noise might be large at times. All these can cause occasional low instantaneous signal-to-noise ratio in the received signal and result in incorrect estimation of the phase changes during sampling intervals, which is manifested as sudden erroneous jumps in the measured vibration displacement.

In this section, the aforementioned issue in extracting the oscillatory displacement from Doppler radar phase history is analyzed, and the two proposed adaptive algorithms that handle this relevant challenge are detailed.

A. Adaptive Low-Pass Filtering Algorithm

The complex representation of the baseband signals after combining the I/Q responses can be written as

$$\begin{aligned} y(t) &= I(t) + jQ(t) \\ &= \sum_{p=-\infty}^{\infty} J_p\left(\frac{4\pi m}{\lambda}\right) e^{\Delta\phi(t)} e^{jp\omega_0 t} + v(t) \end{aligned} \tag{6}$$

where $v(t)$ represents the noise term. On the other hand, the sampled version of (6) can be represented as

$$y(n\Delta t) = \sum_{p=-\infty}^{\infty} C_p e^{jp\omega_0(n\Delta t)} + v(n\Delta t) \tag{7}$$

where Δt is the sampling interval and $n = 0, 1, 2, \ldots, N-1$ with N being the sampled data length. The complex coefficient C_p is equal to $J_p(4\pi m/\lambda)e^{\Delta\phi(t)}$.

The data sequence $[y(n\Delta t)]_{n=0}^{N-1}$ in (7) consists of an infinite number of sinusoidal components. Therefore, it would not be feasible to obtain an infinite number of unknowns $C_p's$ and $p\omega_0's$ from a finite number of data samples. However, the power of the harmonic components decays rapidly, so it can be assumed that $[y(n\Delta t)]_{n=0}^{N-1}$ is composed of k strongest sinusoids by neglecting the weak sinusoidal components. The value of k depends on the motion amplitude detected by the Doppler radar [33]. Hence, (7) can be simplified as

$$y_n = \sum_{p=0}^{k} C_p e^{jp\omega_0(n\Delta t)} + v_n \tag{8}$$

where v_n is the sum of the noise term and the neglected weak sinusoidal components.

To include only the k strongest components in the phase demodulation of the Doppler radar baseband signals and precisely attenuate the insignificant high-frequency components, a low-pass filter is applied to both the I and Q baseband signals. The ALFA is based on the instantaneous vibration amplitude of the mast arm, which decides the number, k, of the strongest sinusoidal components of the I/Q baseband signals. In particular, the cutoff frequency of the low-pass filter (ω_c) is chosen to be slightly higher than the frequency of the weakest observable harmonic component among the k strongest ones (ω_{th}). Therefore, a circle fitting algorithm, whose window size in seconds is empirically determined as $Tcf = 2\pi/\omega_0$, is used to perform the dc offset calibration before the arctangent demodulation.

To demonstrate the effectiveness of the low-pass filtering, white Gaussian noise (WGN) was added to 60 s of computer-generated baseband signals. The dominant signal amplitude is around 44 dB above the noise floor on the FFT spectrum for 60-s FFT window size and 1000-Hz sampling frequency. The 1.0-Hz vibration equation is expressed as $x(t) = 10{\cdot}\sin(2\pi\,\mathrm{t})$, where x and t refer to displacement in centimeter and time in second, respectively. In this simulation, the cutoff frequency of the low-pass filter was set to 31 Hz, slightly higher than the frequency of the weakest sinusoidal component, as shown in Fig. 2(a). The arctangent demodulated displacement is shown in Fig. 2(b). Several jumps are introduced. On the other hand, in Fig. 2(c), the abrupt jumps are removed, since the motion amplitude remained unchanged.

The flowchart in Fig. 3 depicts the automated version of the low-pass filtering (ALFA) that adaptively changes its relevant parameters based on the features of the examined data set. The algorithm only requires as input the baseband signals, the carrier frequency, the sampling frequency, and the window size in seconds for the circle fitting subroutine. The angular dominant frequency of the analyzed motion is calculated as the lowest frequency of the structure motion. If jumps are detected after the first iteration, the algorithm stops, and an accurate displacement is provided. However, if jumps are identified, more iterations must be performed. It should be noted that the correct acquisition of ω_0 is crucial for the convergence of the ALFA. If Tcf is not correctly calculated, the ALFA will be unable to demodulate the I/Q baseband signals, resulting in the algorithm to stuck in a permanent loop.

Analytically, the routine always identifies jumps when the average of the first half of the demodulated baseband signals differs at least 2 mm from the average of the second half.

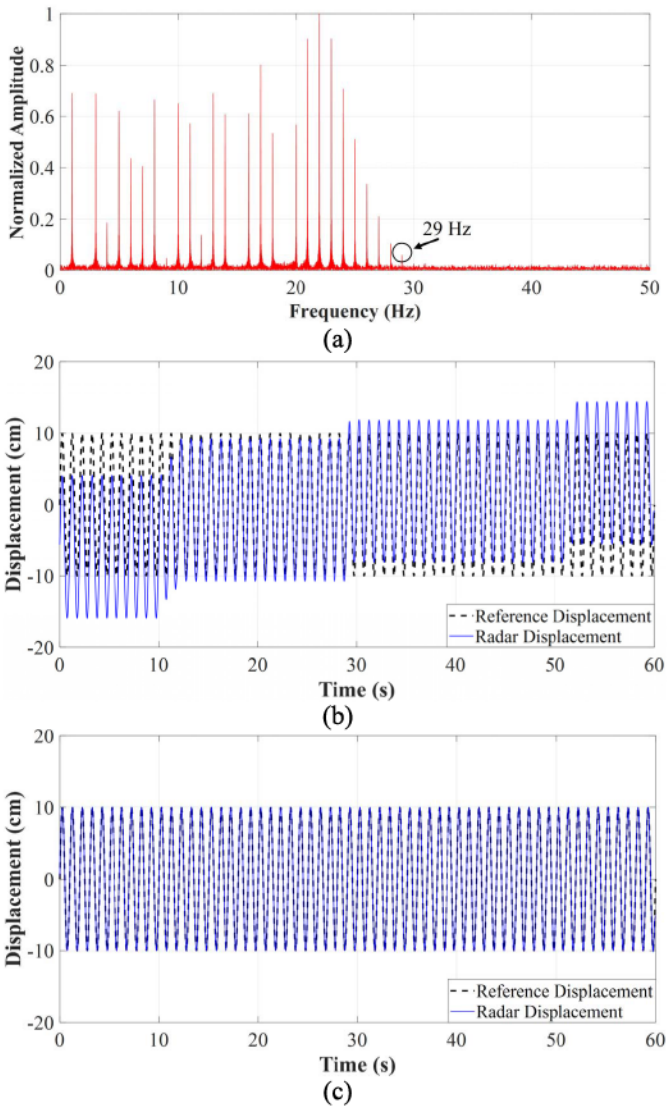

Fig. 2. Simulation results. (a) Spectra of the baseband signals. (b) Arctangent demodulated displacement. (c) Displacement demodulated by the low-pass filtering strategy.

The corresponding steps to automatically derive the calibrated displacement in the occurrence of the latter situation are presented in the following.

1) The time extension of the recorded radar signal, which is referred to as the variable t_{final} on the flowchart, is calculated based on the sampling frequency. Initially, the variable t_{start} is set to zero, and t_{end} assumes the value of t_{final}.
2) As sudden jumps are detected, t_{end} will assume the mean value between t_{start} and the previous value of t_{end} for each iteration. However, t_{start} remains unchanged.
3) The algorithm runs until no jump is identified or the difference ($t_{\text{end}} - t_{\text{start}}$) comes to a minimum value, by which the Doppler radar data cannot be processed. In the occurrence of either situation, an intermediate demodulated displacement is generated.
4) When no jump is encountered in an intermediate demodulated displacement, t_{start} assumes the last assigned value of t_{end}, and t_{end} becomes t_{final}.

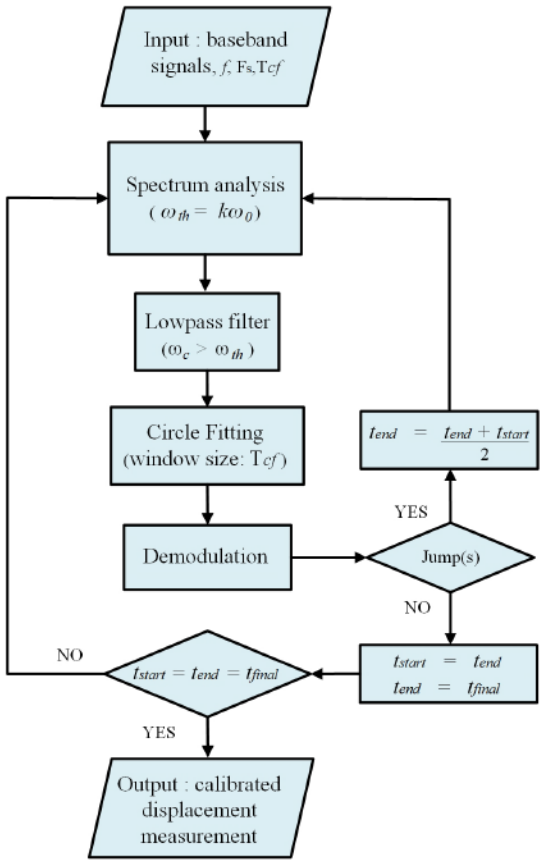

Fig. 3. Flowchart for the proposed adaptive low-pass filtering algorithm.

5) The algorithm continues to run until the difference ($t_{\text{start}} - t_{\text{end}}$) vanishes, which only happens when $t_{\text{start}} = t_{\text{end}} = t_{\text{final}}$.
6) Finally, the intermediate calibrated displacement measurements are concatenated, and the entire Doppler radar calibrated displacement measurement is provided.

To avoid longer processing time delay, since SHM applications require the analysis of a large amount of data, such as month-long data, the length of the I/Q signals fed as input in the ALFA should be adequately chosen depending on the employed digital signal processor.

To illustrate the effectiveness of the ALFA, a varying-amplitude motion was generated in computer simulation. WGN was added to 200 s of simulated baseband signals. The dominant signal amplitude is about 33 dB above the noise floor on the FFT spectrum for 200-s FFT window size and 1000-Hz sampling frequency. In this simulation, since the motion amplitude changes as time progresses, the cutoff frequency of the low-pass filter cannot be fixed. In Fig. 4(a), the spectrogram of the baseband signals is depicted. In addition, the frequencies of harmonic components used as references inside the ALFA are highlighted (70, 38, and 20 Hz). It should be noted that the higher order harmonic components vanish because of the damping amplitude motion. The arctangent demodulated displacement exhibited in Fig. 4(b) presents several jumps. In Fig. 4(c), the low-pass filtering fails in removing the sudden jumps. To adjust the uncalibrated displacement shown in Fig. 4(b), the ALFA eventually separated it into three

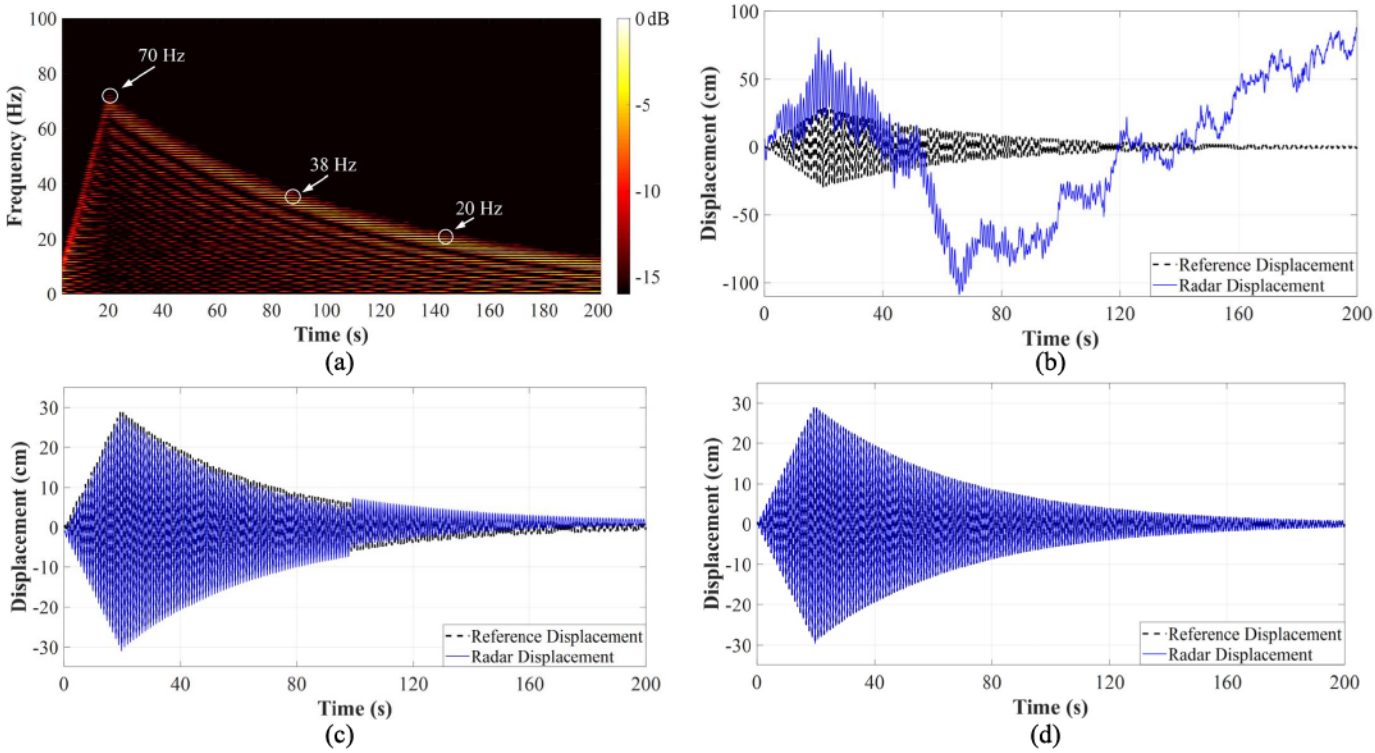

Fig. 4. Simulation results. (a) Spectrogram of the baseband signals. The frequencies of the harmonic components used as references to calculate ω_c inside the ALFA are highlighted. (b) Arctangent demodulated displacement. (c) Displacement demodulated by the low-pass filtering. (d) Displacement demodulated by the ALFA.

sections and then applied a low-pass filter to the baseband signals of each section. The first section is low-pass filtered with a cutoff frequency equal to 72 Hz. For the second section, the cutoff frequency assumes a value of 40 Hz. Finally, the third section is low-pass filtered with a cutoff frequency of 22 Hz. Apparently, the cutoff frequencies adaptively assumed the values of 72, 40, and 22 Hz, which are slightly higher than the frequencies highlighted in Fig. 4(a). In fact, the implemented MATLAB code of the ALFA defines the cutoff frequencies of the low-pass filters as 2 Hz plus the nearest integer greater than or equal to the frequencies of the weakest harmonic components in each separated section. The value of 2 Hz is chosen to ensure that no harmonic component necessary to properly demodulate the signal is attenuated by the low-pass filter. In contrast, Fig 4(d) shows the displacement demodulated by the ALFA. All jumps are eliminated.

B. Adaptive Joint Signal Processing Algorithm

The joint signal processing algorithm (JSPA) consists of a median filter and a revised circle fitting routine followed by the conventional arctangent demodulation method to remove jumps from Doppler radar displacement signals [30]. The median filter is considered to reduce the excessive noise level. In addition, it has an advantage in preserving edges of a waveform and is less vulnerable to a single corrupted sampling point, in comparison with the mean filter [34]. However, its window length must be carefully chosen so that the I/Q baseband signals may not suffer from severe attenuation, especially in high amplitude motion situations.

However, since there may be jumps omitted by a median filter, a revised circle fitting subroutine, which is a circular interpolation subroutine is adopted to correct eventual disparities after the conventional circle fitting processing, so that the remaining jumps are removed as well. In fact, in the case of low SNR, some sampling points may lie close to the origin of the constellation graph, and they tend to move randomly around the four quadrants. Then, its phase angle fluctuates considerably. The circular interpolation subroutine identifies the points in the constellation graph whose radius is less than a specific threshold (e.g., $r_{\mathrm{TH}} = 0.3$) and replaces each of the deviant points by the midpoint of the line segment connecting its two neighboring points, making the absolute phase angle differences smoother. Furthermore, the revised circle fitting routine contributes to reducing the power level of the flicker noise. A simulation is conducted to illustrate the performance of the joint signal processing calibration method. WGN was added to 60 s of computer-generated baseband signals. The dominant signal amplitude is around 44 dB above the noise floor on the FFT spectrum for 60-s FFT window size and 1000-Hz sampling frequency. The amplitude motion is 10 cm, and the frequency of the motion is 1.0 Hz. Fig. 5 exhibits the results of the simulation and the performance of the JSPA. Fig. 5(a) shows the arctangent demodulated displacement. Several jumps are introduced due to the instantaneous noise level. In Fig. 5(b), it can be noted that most jumps are removed by the median filter with a sliding window whose length is equal to 3. The median filter performs two operations: calculating the median value of the three sampling points

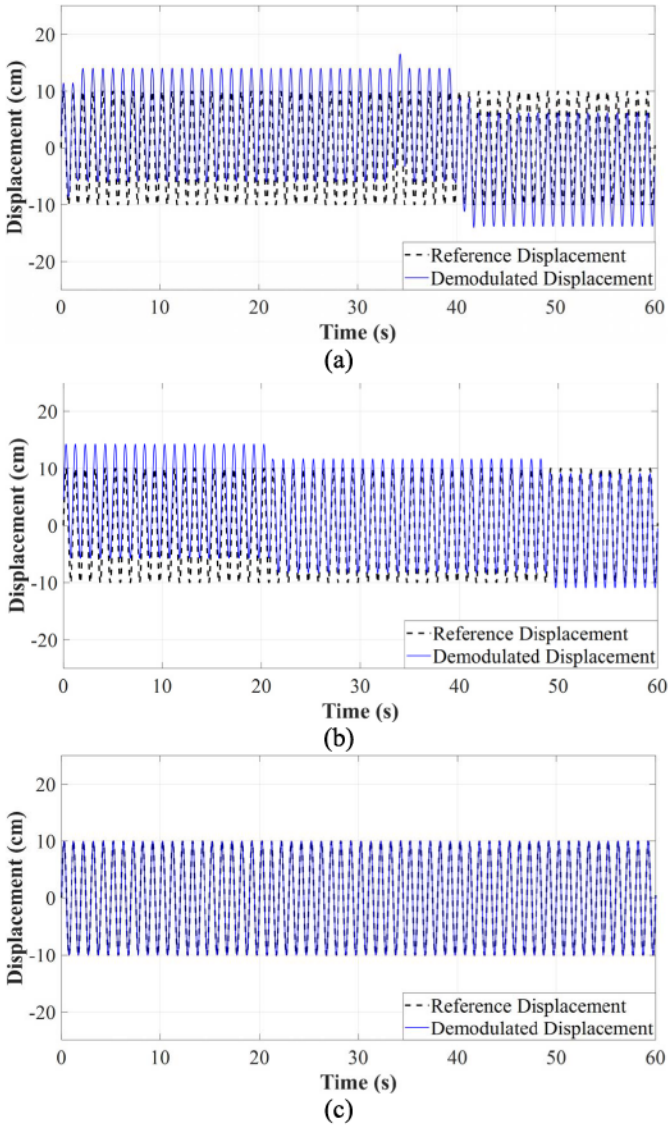

Fig. 5. Simulation results. (a) Arctangent demodulated displacement. (b) Arctangent demodulated displacement with median filter. (c) Displacement demodulated by the JSPA.

inside the window and making the middle element of the three-point array equal to the median value. To eliminate the remaining jumps, the revised circle fitting with a threshold radius of 0.3 is adopted to replace the severely corrupted sampling points. The calibrated displacement is shown in Fig. 5(c).

In order to employ the automated version of the JSPA, the window length of the median filter must be automatically adjusted based on the existence or nonexistence of jumps in the demodulated vibration measurement. As the median filter is a nonlinear filter, it turns out that impulse response and frequency analysis have no significance, and thus, the adaptive window length must be chosen by a trial-and-error process. Fortunately, the attenuation of the baseband signals will be severe for a wide window length [35], [36]. Because of that, an upper threshold value can be determined based on the sampling frequency. As a rule of thumb, for the 1000-Hz sampling frequency, n_{TH} is 19, whereas for 200-Hz sampling

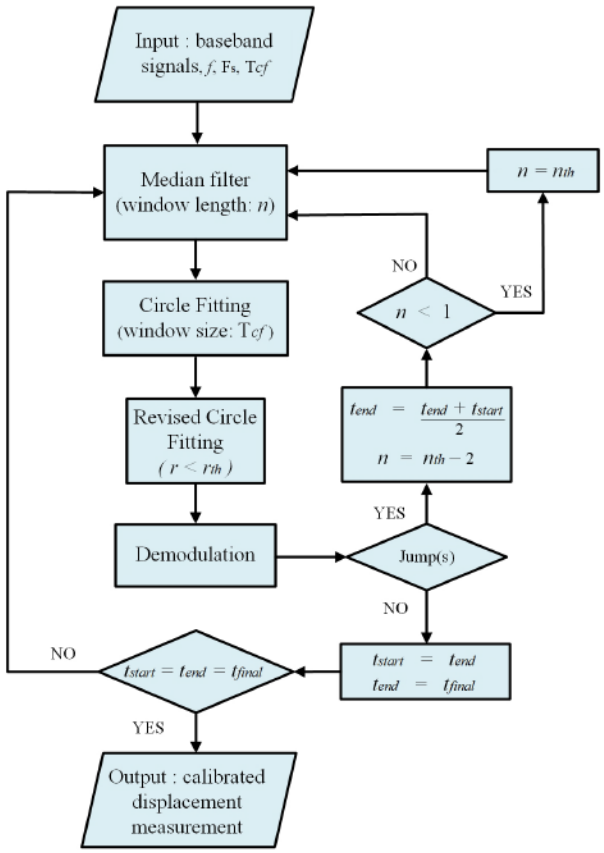

Fig. 6. Flowchart for the proposed AJSPA.

frequency, setting n_{TH} to 5 reveals a proper choice. Moreover, when the revised circle fitting routine is applied, it is found that a good choice of the threshold value for the radius should be 0.3 and 0.1, for the 1000- and 200-Hz sampling rates, respectively, during the displacement calibration of Doppler radar data sets.

The flowchart showing the adaptive JSPA (AJSPA) is exhibited in Fig. 6. The algorithm only requires as input the baseband signals, the carrier frequency, the sampling frequency, and the window size in seconds of the circle fitting subroutine. The angular dominant frequency of the displacement is not needed. Based on the sampling frequency, the baseband response's time extension value is assigned to t_{final}. Initially, t_{start} is set to zero, and t_{end} is equal to t_{final}. If there are no jumps in the demodulated vibration measurement after the first iteration, accurate displacement can be directly obtained. On the other hand, if jumps are identified, the steps below are necessary to automatically derive the calibrated displacement.

1) The variable t_{end} will assume the average value between t_{start} and the previous value of t_{end} for each iteration. In addition, the window length of the median filter (n) will be reduced to $n-2$. If n starts to assume negative values, it will be reset to n_{TH}. However, t_{start} remains unchanged.
2) The algorithm runs until no jumps are identified or the difference ($t_{\mathrm{end}} - t_{\mathrm{start}}$) comes to a minimum value, by which the Doppler radar data cannot be processed.

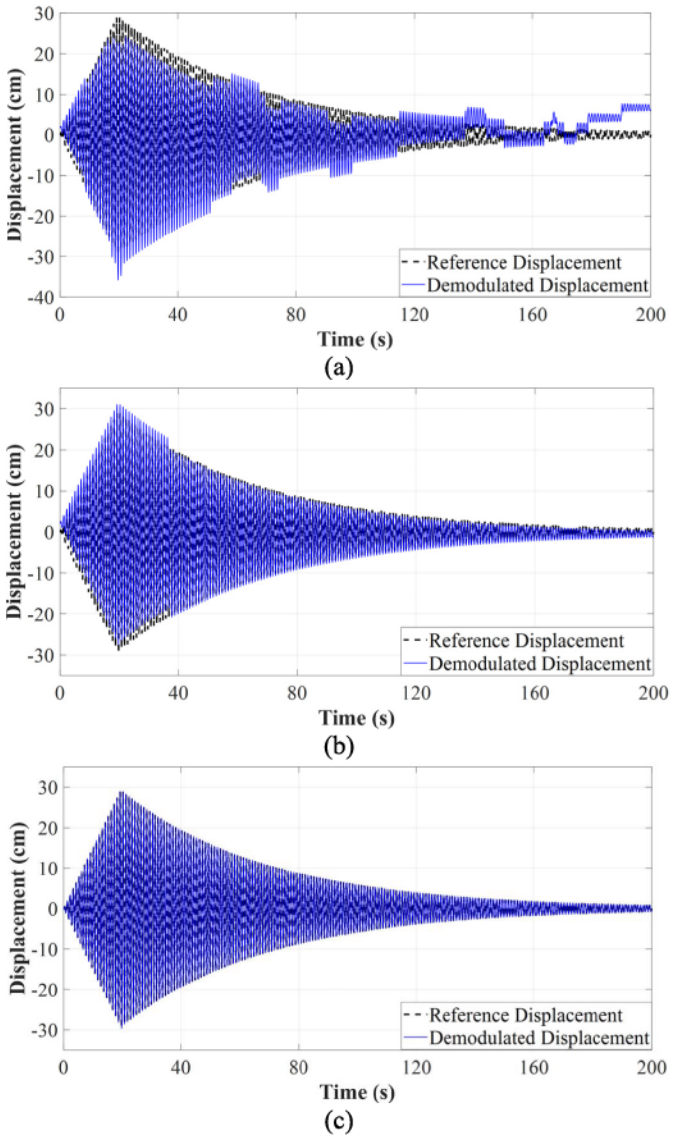

Fig. 7. Simulation results. (a) Arctangent demodulated displacement. (b) Displacement demodulated by the JSPA. (c) Displacement demodulated by the AJSPA.

In the occurrence of either situation, an intermediate demodulated displacement is generated.

3) When no jumps are encountered in an intermediate demodulated displacement, t_{start} assumes the last assigned value of t_{end} and t_{end} becomes t_{final}.
4) The algorithm continues to run until the difference $(t_{\text{start}} - t_{\text{end}})$ vanishes, which only happens if $t_{\text{start}} = t_{\text{end}} = t_{\text{final}}$.
5) Finally, the intermediate calibrated displacement measurements are concatenated, and the entire Doppler radar calibrated displacement measurement is provided.

To exemplify the advantage of the AJSPA over the JSPA, a varying-amplitude motion was computer-generated. WGN was added to 200 s of computer-generated baseband signals. The dominant signal amplitude is about 40 dB above the noise floor on the FFT spectrum for 200-s FFT window size and 1000-Hz sampling frequency. In this simulation, the arctangent demodulated displacement is shown in Fig. 7(a).

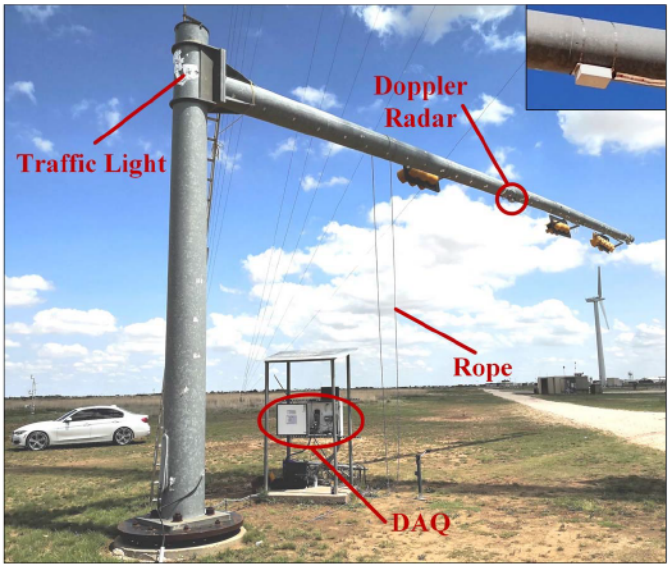

Fig. 8. Experimental setup with the Doppler radar sensor enclosure shown in the inset (from [30]).

Various jumps are introduced. In Fig. 7(b), the JSPA with $n = 3$ and $r_{\text{TH}} = 0.3$ fails in removing the abrupt jumps since the amplitude motion changes as time progresses. Fig 7(c), however, shows the calibrated displacement measurement obtained by the AJSPA.

IV. Experiment Results

To validate the effectiveness and robustness of both approaches in the application of Doppler radars for SHM, a 5.8-GHz radar is used to monitor the motion of a traffic support structure, which consists of a 12-m horizontal mast arm and a 6-m vertical pole. In the experiments, the horizontal arm was manually excited by pulling a rope attached to it. When the vibration reached certain amplitudes, the manual excitation was stopped, and the vibration was allowed to decay freely. The vibration was measured by the radar, which is housed in a plastic enclosure and mounted near the tip of the pole. In the meantime, the vibration was detected by a conventional triaxial dc-response accelerometer of ± 4g in the measurement range that was mounted on the arm at the same axial location as the radar. Both the I/Q channels of the radar and the channels of the accelerometer were sampled by a National Instrument NI-9239 voltage input module on a CompactRIO platform, which was our data acquisition system (DAQ). To investigate the impact of sampling frequency on the measurement quality, some records were sampled at 1000 Hz, while others were sampled at 200 Hz. Fig. 8 shows the experimental setup.

The displacement calibration methods presented in Section III were programmed in MATLAB to process the Doppler radar's signals. Fig. 9(a) and (b) shows the spectra of the baseband signals and the conventional demodulated displacement, respectively, for one of the recorded data sets. The dominant frequency is 1.04 Hz and the weakest sinusoidal component is identified at 40.5 Hz, as shown in Fig. 9(a). Due to low SNR at times for the recorded I/Q

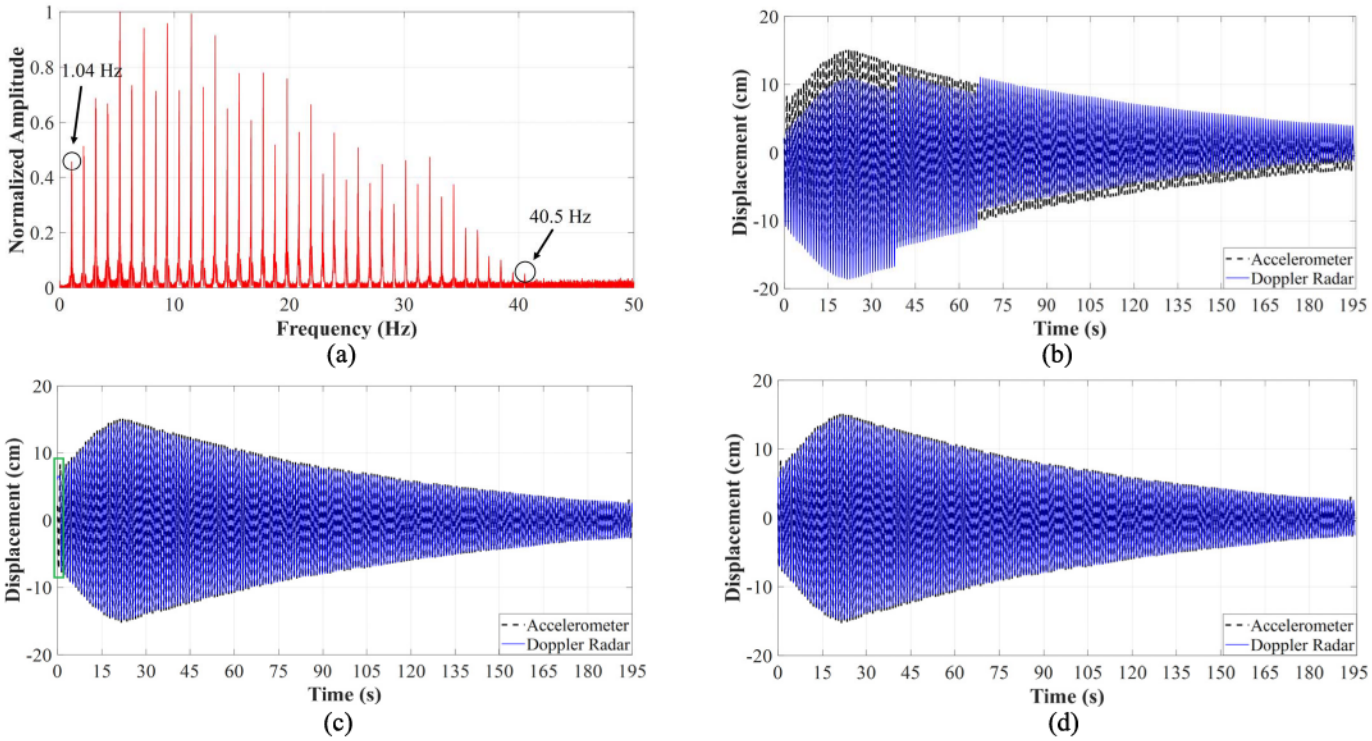

Fig. 9. Experimental results. (a) Spectra of the baseband signals. (b) Demodulated displacement using conventional arctangent demodulation. (c) Demodulated displacement using low-pass filtering. Discontinuities are highlighted at the first instants. (d) Demodulated displacement using the JSPA.

baseband signals, several jumps are seen at the arctangent demodulated displacement, as shown in Fig. 9(b).

The I/Q sinusoidal components of the baseband signals are low-pass filtered with a cutoff frequency of 42 Hz. Fig. 9(c) plots the Doppler radar displacement measurement obtained using the low-pass filtering displacement calibration method and the reference, which is the displacement estimated by numerically integrating the corresponding accelerometer response twice and high-pass filtering the result of each step of integration with a cutoff frequency of 0.5 Hz. A discontinuity in the demodulated displacement is seen in the first instance. The root-mean-square (rms) error between the low-pass filtering displacement measurement and the reference is 0.263 cm.

On the other hand, Fig. 9(d) shows the radar displacement measurement obtained after the application of the JSPA, which incorporates a median filter with a fixed window length of 3 and a revised circle fitting with a threshold radius of 0.1. The reference, which is the ground truth, is also included in this graph. Compared with the demodulated displacement using the conventional arctangent demodulation, the abrupt jumps are eliminated by the JSPA. The rms error between the radar displacement measurement obtained with the application of the JSPA and the ground truth is 0.283 cm.

To have a displacement calibration method appropriate to interrogate in real time the status of the traffic signal's mast arm, the adaptive versions of both the low-pass filtering and the JSPA can be implemented according to the steps outlined in Section III. An example is provided in the following to illustrate the advantages of the automated versions of the algorithms over the versions with fixed parameters. Fig. 10 shows the experimental results of the displacement measurement obtained from a 326-s long data set. As the motion amplitude had reached 20 cm, several sinusoidal components appeared in the baseband signals' spectrogram, as shown in Fig. 10(a). The frequency of the weakest sinusoidal component and the frequency of other harmonic components used as reference inside the ALFA are highlighted. Fig. 10(b) shows the displacement retrieved after applying the conventional arctangent demodulation algorithm. Although the number of jumps in the demodulated Doppler radar signal is only one for the first 240 s, as time elapses and motion amplitude decreases, the SNR deteriorates, causing an increment in the number of jumps. The direct application of the low-pass filtering calibration strategy to the entire data set, with the low-pass filter's cutoff frequency fixed in 49 Hz, does not remove completely the sudden bounces, as shown in Fig. 10(c). Since the motion amplitude changes continuously as time progresses, the number of sinusoidal components on the spectra of the Doppler radar baseband signals may decrease or increase. As a result, the low-pass filter with the fixed cutoff frequency becomes ineffective. Fig. 10(d) shows the displacement measurement based on the radar signals with the direct application of the JSPA with a fixed sliding window length (n) of three sampling points for the median filter and a threshold value for the radius of 0.1 on the revised circle fitting subroutine. The accelerometer displacement measurement is also included in this graph. Because of the unvarying window length, the median filter attenuates part of the high-frequency sinusoidal components, which is demonstrated by the severe displacement distortion when its amplitude reaches about 20 cm.

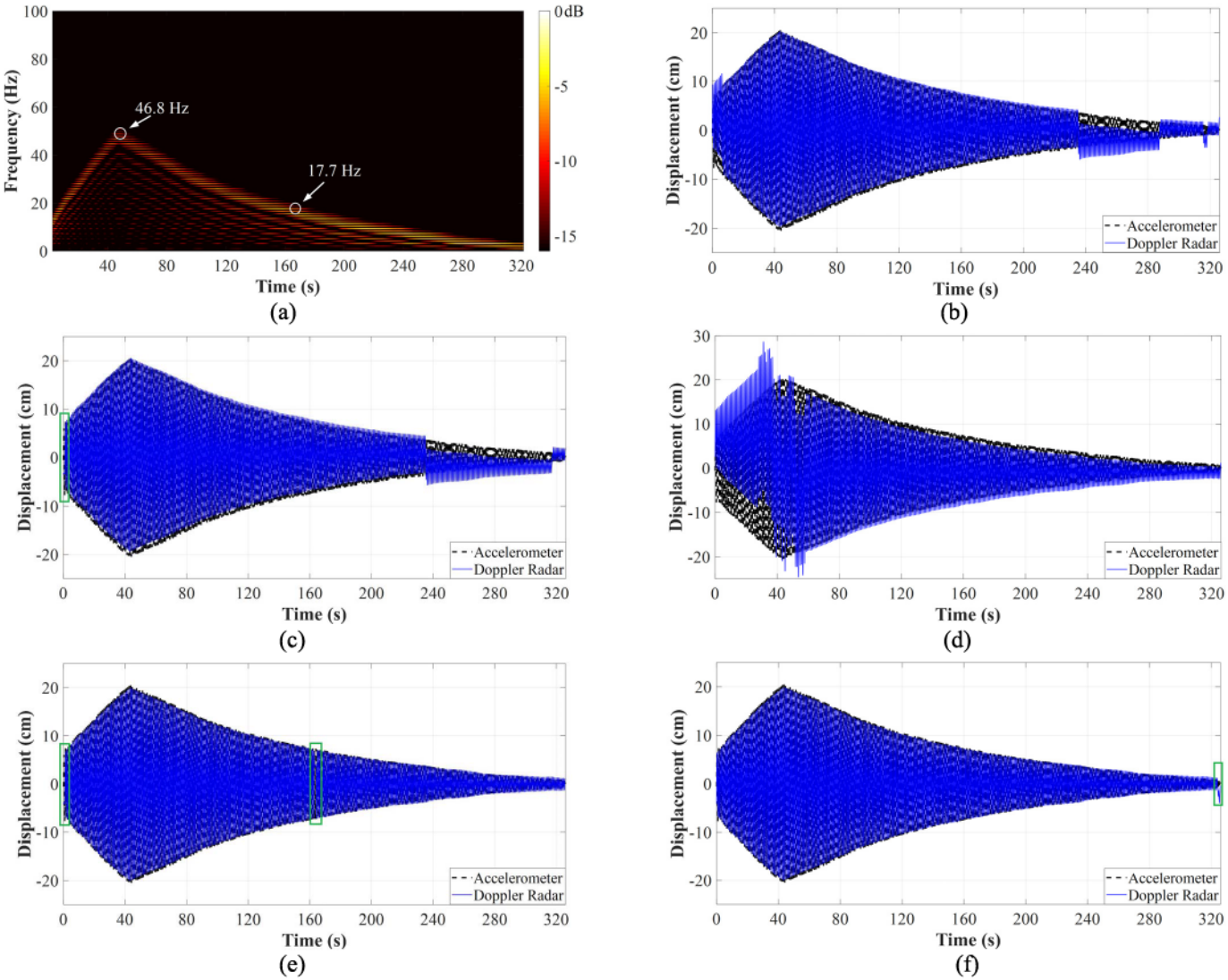

Fig. 10. Experimental results. (a) Spectrogram of the baseband signals. The frequencies of the harmonic components used as references to calculate ω_c inside the ALFA are highlighted. (b) Demodulated displacement using conventional arctangent demodulation. (c) Demodulated displacement using the low-pass filtering. Discontinuities are highlighted. (d) Demodulated displacement using the JSPA. (e) Demodulated displacement using the ALFA. Discontinuities are highlighted. (f) Demodulated displacement using the AJSPA. A discontinuity is highlighted.

In contrast to the previous approaches, Fig. 10(e) and (f) shows the displacement measurements after applying the ALFA and the AJSPA, respectively. Since both methods adaptively modify the key parameters based on the motion features, the sudden jumps are removed from the calculated Doppler radar displacements. Although the displacement measurements in both figures are mostly close to the ground truth, distortions can still be found. As highlighted in Fig. 10(e), the sinusoidal displacement measurement is interrupted by a discontinuity at multiple instants. The discontinuity is included during the intermediate process of cutting apart the displacement measurement that still has abrupt jumps. Then, a new calibration is performed using adaptive values for the key parameters of the ALFA. In contrast, in Fig. 10(f), there is no discontinuity at the first instance. However, when the SNR considerably deteriorates, especially in low amplitude motions, the discontinuities appear, as it is exhibited in Fig. 10(f). The rms error between the ALFA displacement measurement and the accelerometer displacement measurement is 0.465 cm, and the rms error between the AJSPA displacement measurement and the accelerometer displacement measurement is 0.445 cm.

V. Further Discussion

To further understand the two proposed automated algorithms, it is critical to compare their accuracy and computational complexity. The accuracy of each displacement calibration algorithm depends on the characteristics of the measured baseband signals, which are affected by the measurement conditions. Higher noise levels and clutters tend to worsen the measurement accuracy. On the other hand, computational power consumption is a concern in practical radar applications and in SHM applications as the analysis of large amount of data is needed. Therefore, low latency on signal processing plays a critical role.

TABLE I
RADAR MEASUREMENT ACCURACY

Data set	Length (s)	Sampling rate (Hz)	RMS error (cm) ALFA	AJSPA
1	145.88	200	0.315	0.381
2	193.35	200	0.263	0.283
3	272.79	200	0.387	0.422
4	326.00	200	0.465	0.445
5	20.10	1000	0.293	0.315
6	193.87	1000	0.265	0.277
7	185.34	1000	0.315	0.275

TABLE II
COMPUTATIONAL COMPLEXITY

Data set	Sampling rate (Hz)	Latency (s)/ n°. of iterations ALFA	AJSPA
1	200	0.267/1	0.390/3
2	200	0.406/1	0.397/2
3	200	1.622/2	1.053/3
4	200	1.798/2	1.016/3
5	1000	0.156/1	0.295/2
6	1000	5.552/1	2.625/2
7	1000	5.443/1	1.008/1

A. Accuracy

The accuracy of different displacement calibration methods is investigated by comparing the Doppler radar displacement and the accelerometer displacement measurements and then calculating the rms error for each proposed algorithm, which are listed in Table I for seven experimental data sets sampled with 200- and 1000-Hz rates. The length of the data sets varies from 20.1 to 326 s. The displacement measurement error is not only due to environmental noise but also due to radar system noise, such as quantization noise and electronic noise. The data sets presented an rms error between 0.26 and 0.47 cm. As shown in Fig. 10(e) and (f), the displacement measurements calculated by both the ALFA and the AJSPA exhibited distortions. From the calculated rms errors, it is not easy to conclude which one is superior in terms of accuracy. However, even with the introduced noises and the existing distortions in the displacement measurement, the Doppler radar sensor aided with either algorithm provided a subcentimeter measurement accuracy.

B. Computational Complexity

The assessment of the computational complexity was accomplished by recording the time required for MATLAB to complete the displacement calibration for the seven data sets used in Section V-A. The elapsed time was estimated with the MATLAB "timeit" operand. Table II shows the latency and the number of iterations required by each data set to have most of its sudden jumps removed. It should be noted that the latency required by the AJSPA is shorter than the one required by the ALFA, especially for longer data sets. This is due to the demanding spectral analysis subroutine present in the ALFA, although the AJSPA needed more iterations to remove the sudden jumps for some data sets. On the other hand, the spectral analysis subroutine helps ALFA to be more effective than the AJSPA on calibrating simulated and experimental data with considerably deteriorated SNR.

VI. CONCLUSION

In this article, two algorithms to remove abrupt jumps in phase-demodulated Doppler radar data from field SHM applications are introduced. A series of simulations and experimental measurements has demonstrated the effectiveness of both methods. A deployment strategy has been provided for both algorithms, confirmed by experimental measurements, and compared in terms of accuracy and computational cost. Subcentimeter measurement accuracy is achieved. The proposed adaptive strategies may be used for the analysis of long-term Doppler radar baseband responses by monitoring small amplitude motions. Future research may consider the use of the nonlinear radar technology, which has demonstrated clutter rejection capability in the presence of multiple clutters, to achieve robust detection at the presence of moving objects such as vehicles and humans in the scene [37].

REFERENCES

[1] C. Farrar and K. Worden, "An introduction to structural health monitoring," *Phil. Trans. Roy. Soc. A, Math., Phys. Eng. Sci.*, vol. 365, no. 1851, pp. 303–315, 2007.
[2] D. Zuo and C. W. Letchford, "Wind-induced vibration of a traffic-signal-support structure with cantilevered tapered circular mast ARM," *Eng. Struct.*, vol. 32, no. 10, pp. 3171–3179, Oct. 2010.
[3] D. Jayawardana, S. Kharkovsky, R. Liyanapathirana, and X. Zhu, "Measurement system with accelerometer integrated RFID tag for infrastructure health monitoring," *IEEE Trans. Instrum. Meas.*, vol. 65, no. 5, pp. 1163–1171, May 2016.
[4] J. Fang and T. Wen, "A wide linear range eddy current displacement sensor equipped with dual-coil probe applied in the magnetic suspension flywheel," *Sensors*, vol. 12, no. 8, pp. 10693–10706, 2012.
[5] P. Giri and S. Kharkovsky, "Detection of surface crack in concrete using measurement technique with laser displacement sensor," *IEEE Trans. Instrum. Meas.*, vol. 65, no. 8, pp. 1951–1953, Aug. 2016.
[6] S. Cao, I. Kajiwara, X. Li, and N. Hosoya, "Structural health monitoring based on laser excitation vibration test and wavelet transform," in *Proc. 11th Int. Conf. Sens. Technol. (ICST)*, Sydney, NSW, Australia, Dec. 2017, pp. 1–6.
[7] D. Feng, M. Feng, E. Ozer, and Y. Fukuda, "A vision-based sensor for noncontact structural displacement measurement," *Sensors*, vol. 15, no. 7, pp. 16557–16575, 2015.
[8] Y. Fukuda, M. Q. Feng, Y. Narita, S. Kaneko, and T. Tanaka, "Vision-based displacement sensor for monitoring dynamic response using robust object search algorithm," *IEEE Sensors J.*, vol. 13, no. 12, pp. 4725–4732, Dec. 2013.
[9] T. Khuc and F. N. Catbas, "Completely contactless structural health monitoring of real-life structures using cameras and computer vision," *Struct. Control Health Monitor.*, vol. 24, no. 1, Jan. 2017, Art. no. e1852.
[10] C. Li, J. Lin, and Y. Xiao, "Robust overnight monitoring of human vital signs by a non-contact respiration and heartbeat detector," in *Proc. Int. Conf. IEEE Eng. Med. Biol. Soc.*, Aug. 2006, pp. 2235–2238.
[11] A. Singh, S. S. K. Lee, M. Butler, and V. Lubecke, "Activity monitoring and motion classification of the lizard Chamaeleo jacksonii using multiple Doppler radars," in *Proc. Annu. Int. Conf. IEEE Eng. Med. Biol. Soc.*, Aug. 2012, pp. 4525–4528.
[12] C. Gu *et al.*, "Accurate respiration measurement using DC-coupled continuous-wave radar sensor for motion-adaptive cancer radiotherapy," *IEEE Trans. Biomed. Eng.*, vol. 59, no. 11, pp. 3117–3123, Nov. 2012.

[13] H. Zhao, H. Hong, L. Sun, Y. Li, C. Li, and X. Zhu, "Noncontact physiological dynamics detection using low-power digital-IF Doppler radar," *IEEE Trans. Instrum. Meas.*, vol. 66, no. 7, pp. 1780–1788, Jul. 2017.

[14] S. M. A. Tayaranian Hosseini and H. Amindavar, "A new ka-band Doppler radar in robust and precise cardiopulmonary remote sensing," *IEEE Trans. Instrum. Meas.*, vol. 66, no. 11, pp. 3012–3022, Nov. 2017.

[15] C. Atzeni, A. Bicci, D. Dei, M. Fratini, and M. Pieraccini, "Remote survey of the leaning tower of Pisa by interferometric sensing," *IEEE Geosci. Remote Sens. Lett.*, vol. 7, no. 1, pp. 185–189, Jan. 2010.

[16] J. A. Rice, C. Gu, C. Li, and S. Guan, "A radar-based sensor network for bridge displacement measurements," *Proc. SPIE*, vol. 8345, Apr. 2012, Art. no. 83450I.

[17] T. A. Stabile, A. Perrone, M. R. Gallipoli, R. Ditommaso, and F. C. Ponzo, "Dynamic survey of the musmeci bridge by joint application of ground-based microwave radar interferometry and ambient noise standard spectral ratio techniques," *IEEE Geosci. Remote Sens. Lett.*, vol. 10, no. 4, pp. 870–874, Jul. 2013.

[18] M. Diaferio, A. Fraddosio, M. Daniele Piccioni, A. Castellano, L. Mangialardi, and L. Soria, "Some issues in the structural health monitoring of a railway viaduct by ground based radar interferometry," in *Proc. IEEE Workshop Environ., Energy, Struct. Monitor. Syst. (EESMS)*, Jul. 2017, pp. 1–6.

[19] A. Castellano, A. Fraddosio, F. Martorano, G. Mininno, F. Paparella, and M. D. Piccioni, "Structural health monitoring of a historic masonry bell tower by radar interferometric measurements," in *Proc. IEEE Workshop Environ., Energy, Struct. Monitor. Syst. (EESMS)*, Jun. 2018, pp. 1–6.

[20] M. Pieraccini and L. Miccinesi, "An interferometric MIMO radar for bridge monitoring," *IEEE Geosci. Remote Sens. Lett.*, vol. 16, no. 9, pp. 1383–1387, Sep. 2019.

[21] C. Li *et al.*, "A review on recent progress of portable short-range noncontact microwave radar systems," *IEEE Trans. Microw. Theory Techn.*, vol. 65, no. 5, pp. 1692–1706, May 2017.

[22] S. Guan, J. A. Rice, C. Li, Y. Li, and G. Wang, "Structural displacement measurements using DC coupled radar with active transponder," *Struct. Control Health Monitor.*, vol. 24, no. 4, p. e1909, Apr. 2017.

[23] S. Guan, J. A. Rice, C. Li, and N. J. DeMello, "Smart radar sensor network for bridge displacement monitoring," *J. Bridge Eng.*, vol. 24, no. 1, 2019, Art. no. 04018102.

[24] J.-M. Munoz-Ferreras, Z. Peng, Y. Tang, R. Gomez-Garcia, D. Liang, and C. Li, "Short-range Doppler-radar signatures from industrial wind turbines: Theory, simulations, and measurements," *IEEE Trans. Instrum. Meas.*, vol. 65, no. 9, pp. 2108–2119, Sep. 2016.

[25] J. Moll *et al.*, "Radar-based structural health monitoring of wind turbine blades: The case of damage detection," *Struct. Health Monitor.*, vol. 17, no. 4, pp. 815–822, Jul. 2018.

[26] J. Moll *et al.*, "Radar imaging system for in-service wind turbine blades inspections: Initial results from a field installation at a 2mW wind turbine," *Prog. Electromagn. Res.*, vol. 162, pp. 51–60, 2018.

[27] J. Wang, X. Wang, L. Chen, J. Huangfu, C. Li, and L. Ran, "Noncontact distance and amplitude-independent vibration measurement based on an extended DACM algorithm," *IEEE Trans. Instrum. Meas.*, vol. 63, no. 1, pp. 145–153, Jan. 2014.

[28] S. Guan, J. A. Rice, C. Li, and C. Gu, "Automated DC offset calibration strategy for structural health monitoring based on portable CW radar sensor," *IEEE Trans. Instrum. Meas.*, vol. 63, no. 12, pp. 3111–3118, Dec. 2014.

[29] D. Tang, J. Wang, W. Hu, Z. Peng, Y.-C. Chiang, and C. Li, "A DC-coupled high dynamic range biomedical radar sensor with fast-settling analog DC offset cancelation," *IEEE Trans. Instrum. Meas.*, vol. 68, no. 5, pp. 1441–1450, May 2019.

[30] D. V. Q. Rodrigues, Z. Tang, J. Wang, D. Zuo, and C. Li, "Structural health monitoring of a traffic signal support structure based on 5.8-GHz Doppler radar with median filter and revised circle fitting," in *Proc. IEEE Radio Wireless Symp.*, Jan. 2020.

[31] C. Li, Y. Xiao, and J. Lin, "Experiment and spectral analysis of a low-power Ka-band heartbeat detector measuring from four sides of a human body," *IEEE Trans. Microw. Theory Techn.*, vol. 54, no. 12, pp. 4464–4471, Dec. 2006.

[32] B.-K. Park, O. Boric-Lubecke, and V. M. Lubecke, "Arctangent demodulation with DC offset compensation in quadrature Doppler radar receiver systems," *IEEE Trans. Microw. Theory Techn.*, vol. 55, no. 5, pp. 1073–1079, May 2007.

[33] C. Li, J. Ling, J. Li, and J. Lin, "Accurate Doppler radar noncontact vital sign detection using the RELAX algorithm," *IEEE Trans. Instrum. Meas.*, vol. 59, no. 3, pp. 687–695, Mar. 2010.

[34] A. Hamza, P. Luque–Escamilla, J. Martínez-Aroza, and R. Román-Roldán, "Removing noise and preserving details with relaxed median filters," *J. Math. Imag. Vis.*, vol. 11, no. 2, pp. 161–177, 1999.

[35] N. Gallagher and G. Wise, "A theoretical analysis of the properties of median filters," *IEEE Trans. Acoust., Speech, Signal Process.*, vol. 29, no. 6, pp. 1136–1141, Dec. 1981.

[36] V. G. Moshnyaga and K. Hashimoto, "An efficient implementation of 1-D median filter," in *Proc. 52nd IEEE Int. Midwest Symp. Circuits Syst.*, Aug. 2009, pp. 451–454.

[37] A. Mishra and C. Li, "A low power 5.8-GHz ISM-band intermodulation radar system for target motion discrimination," *IEEE Sensors J.*, vol. 19, no. 20, pp. 9206–9214, Oct. 2019.

Davi V. Q. Rodrigues (Student Member, IEEE) received the B.S. degree in communications engineering from the Military Institute of Engineering, Rio de Janeiro, Brazil, in 2017. He is currently pursuing the Ph.D. degree in electrical engineering with Texas Tech University, Lubbock, TX, USA.

From 2009 to 2011, he was with the Brazilian Navy, Rio de Janeiro. In 2013, he became a member of the Brazilian Army, and, in 2017, was commissioned as first lieutenant of the Military Engineers Branch. In the Spring/Summer of 2018, he served in the Southern Military Command, Porto Alegre, Brazil. He joined Texas Tech University, as a Research Assistant in the Fall of 2018. His research interests include biomedical applications of microwave/RF, microwave/millimeter-wave circuits and systems, and wireless sensors. He received the First Place Winner Award of the Student Design Competition for Adaptive Relay Transceiver, and the Second Place Winner Award of the Student Design Competition for High-Sensitivity Motion Radar in the 2019 IEEE MTT-S International Microwave Symposium.

Delong Zuo received the B.S. degree in civil engineering from Chongqing Jiaotong University, Chongqing, China, in 1996, and the Ph.D. degree in civil engineering from Johns Hopkins University, Baltimore, MD, USA, in 2005.

From 2005 to 2006, he was a Post-Doctoral Fellow with Johns Hopkins University. He joined Texas Tech University, Lubbock, TX, USA, in 2006, where he is currently an Associate Professor of civil engineering. His research interests include structural dynamics, structural vibration control, bluff-body aerodynamics, wind loading on structures, and wind–structure interaction.

Ziyan Tang received the B.S. degree in mechanical engineering from Shanghai Jiao Tong University, Shanghai, China, in 2019. He is currently pursuing the M.S. degree in mechanical engineering with the University of Michigan, Ann Arbor, MI, USA.

His research interests include structural health monitoring, fault diagnosis, vibration analysis, and radar signal processing.

Jing Wang (Student Member, IEEE) received the B.S. degree in communication engineering from the Fujian University of Technology, Fuzhou, China, in 2015. She is currently pursuing the Ph.D. degree in electrical engineering with Texas Tech University, Lubbock, TX, USA.

Her current research interests include microwave circuits, wireless RF sensors, and their biomedical applications.

Changzhan Gu (Senior Member, IEEE) received the B.S. and M.S. degrees from Zhejiang University, Hangzhou, China, in 2006 and 2008, the M.S. degree from the University of Florida, Gainesville, FL, USA, in 2010, and the Ph.D. degree from Texas Tech University, Lubbock, TX, USA, in 2013.

He is currently an Associate Professor with the MoE Key Lab of Artificial Intelligence and the MoE Key Lab of Design and EMC of High-Speed Electronic Systems, Shanghai Jiao Tong University (SJTU). He was with Google, Mountain View, CA, USA, where he was involved with radar gesture sensing technology and translating it into consumer hardware products.

Dr. Gu received the IEEE Sensors Council Early Career Technical Achievement Award in 2019, the Okawa Foundation Research Grant in 2019, and the IEEE MTT-S Graduate Fellowship in 2013. He is an Associate Editor of the IEEE TRANSACTIONS ON BIOMEDICAL CIRCUITS AND SYSTEMS (TBioCAS), the IEEE JOURNAL OF ELECTROMAGNETICS, RF AND MICROWAVES IN MEDICINE AND BIOLOGY (J-ERM) and *IET Microwave, Antenna & Propagation* (MAP).

Changzhi Li (Senior Member, IEEE) received the B.S. degree in electrical engineering from Zhejiang University, Hangzhou, China, in 2004, and the Ph.D. degree in electrical engineering from the University of Florida, Gainesville, FL, USA, in 2009.

In Summer of 2007–2009, he was first with Alereon Inc., Austin, TX, USA, and then Coherent Logix Inc., Austin, where he was involved in ultra-wideband (UWB) transceivers and software-defined radio, respectively. In 2009, he joined Texas Tech University, Lubbock, TX, USA, as an Assistant Professor, where he became an Associate Professor in 2014. His research interests include biomedical applications of microwave technology, wireless sensors, and RF/analog circuits.

Dr. Li was a recipient of the IEEE Microwave Theory and Techniques Society (MTT-S) Outstanding Young Engineer Award, the IEEE Sensors Council Early Career Technical Achievement Award, the ASEE Frederick Emmons Terman Award, the IEEE-HKN Outstanding Young Professional Award, the NSF Faculty Early CAREER Award, and the IEEE MTT-S Graduate Fellowship Award. He served as the TPC Co-Chair for the IEEE MTT-S International Microwave Biomedical Conference from 2018 to 2019 and the IEEE Wireless and Microwave Technology Conference from 2012 to 2013. He served as an Associate Editor for the IEEE TRANSACTIONS ON CIRCUITS AND SYSTEMS—II: EXPRESS BRIEFS from 2014 to 2015. He is an Associate Editor of the IEEE TRANSACTIONS ON MICROWAVE THEORY AND TECHNIQUES, the IEEE TRANSACTIONS ON CIRCUITS AND SYSTEMS—I: REGULAR PAPERS, and the IEEE JOURNAL OF ELECTROMAGNETICS, RF AND MICROWAVES IN MEDICINE AND BIOLOGY.